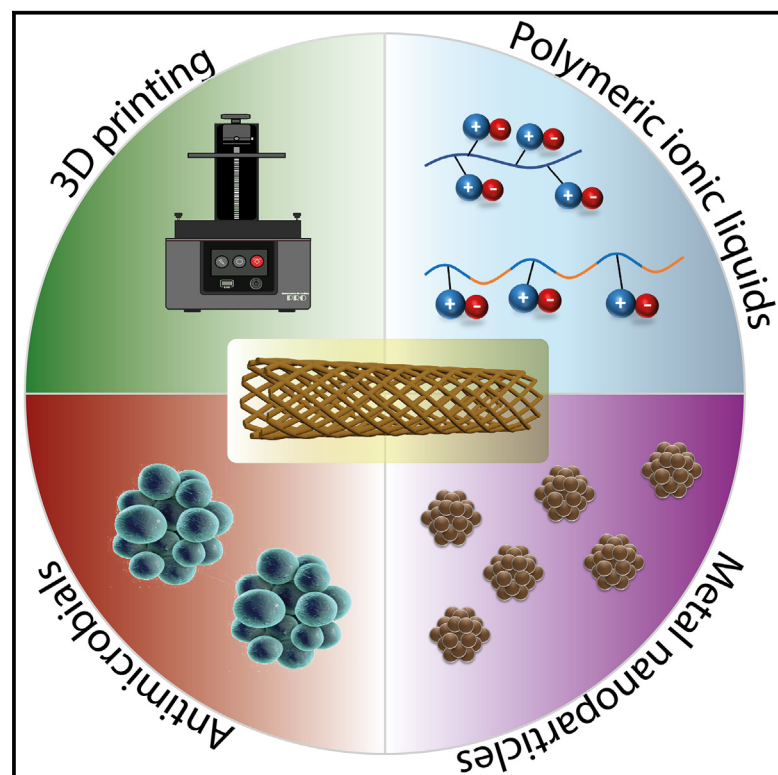# Development of high-resolution 3D printable polymerizable ionic liquids for antimicrobial applications

Graphical abstract

Authors

Sara Miralles-Comins, Marcileia Zanatta, Sonia García Embid, ..., Ignazio Roppolo, Scott G. Mitchell, Victor Sans

Correspondence

sans@uji.es

In brief

New materials and devices based on 3D-printed polymeric ionic liquids with antimicrobial properties are presented.

Highlights

- Innovative copper encapsulation in polymeric ionic liquids with antimicrobial activity

- A medical stent was 3D-printed with high resolution using DLP and MSLA

- The material exhibited 98% bactericidal efficacy against *S. epidermidis*

Develop
3
Prototype with demonstrated applications in relevant environment

CellPress

Device

Article

Development of high-resolution 3D printable polymerizable ionic liquids for antimicrobial applications

Sara Miralles-Comins,[1] Marcileia Zanatta,[1] Sonia García Embid,[2,3] Maria Alleva,[2,3] Annalisa Chiappone,[4] Ignazio Roppolo,[5] Scott G. Mitchell,[2,3] and Victor Sans[1,6,*]

[1]Institute of Advanced Materials (INAM), Universitat Jaume I (UJI), Avenida de Vicent Sos Baynat, s/n, 12071 Castelló de la Plana, Castellón, Spain
[2]Instituto de Nanociencia y Materiales de Aragón (INMA-CSIC/UNIZAR), CSIC-Universidad de Zaragoza, C/Pedro Cerbuna 12, 50009 Zaragoza, Spain
[3]CIBER de Bioingeniería, Biomateriales y Nanomedicina, Instituto de Salud Carlos III, 28029 Madrid, Spain
[4]Dipartimento di Scienze Chimiche e Geologiche, Università di Cagliari, S.S. 554 bivio Sestu, 09042 Monserrato, Italy
[5]Dipartimento di Scienza Applicata e Tecnologia, Politecnico di Torino, C.so Duca degli Abruzzi 24, 10129 Turin, Italy
[6]Lead contact
*Correspondence: sans@uji.es
https://doi.org/10.1016/j.device.2023.100224

THE BIGGER PICTURE In the quest to address global antibiotic resistance, this study pioneers 3D-printable antimicrobial polymeric scaffolds with embedded copper-based nanoparticles. A polymeric formulation based on polymeric ionic liquids has been carefully designed to overcome nanoparticle stabilization challenges, while being optimized for 3D printing. Customized formulations for digital light processing and masked stereolithography-based 3D printing are introduced, resulting in high-resolution materials with potent antimicrobial properties. Successful 3D printing of a device analogous to a medical stent demonstrated their efficacy against the growth of *S. epidermidis* bacteria. This research underscores additive manufacturing's transformative potential for high-resolution devices, contributing significantly to a critical global health concern. It establishes a foundation for diverse antimicrobial solutions, marking a substantial advancement in the field.

SUMMARY

In recent years, 3D printing has undergone a significant transformation, expanding beyond its initial niche applications, such as rapid prototyping and hobbyist projects. This evolution has been characterized by advancements in equipment, software, and, most notably, materials. However, the development of materials that present high-resolution and advanced tunable functionalities is still a challenge. Herein, we report the development of modular 3D-printable antimicrobial polymeric ionic liquid (PIL) scaffolds with *in situ* formation of copper-based nanoparticles within the polymeric matrix (Cu@PILs). A variety of formulations were specially designed and optimized to be printed by digital light processing and masked stereolithography techniques at high resolution. The antimicrobial activity as well as the biocompatibility of the different formulations was tested, changing the monomeric ionic liquid and the photoinitiator. Tailor-made objects were successfully manufactured, and as a demonstrator, a geometry compatible with a medical stent was printed.

INTRODUCTION

In recent years, 3D printing has experienced a remarkable transformation, offering customization and preparation of advanced devices. In this field, polymers can be specially designed to be manufactured by 3D techniques, being of huge interest since traditional polymerization techniques limit the geometries that can be potentially generated.[1] This sophisticated technology enables to directly transfer the unique properties of molecular materials to macroscopic functional devices, rapidly closing the loop between design, manufacture, and application at a relatively low cost.[2] The unprecedented flexibility in design allows to manufacture high-resolution multi-material devices essential to the development of future technologies.[3–5] The inherent tunability of properties in polymeric ionic liquids (PILs) makes them an incredibly intriguing class of materials for 3D printing.

PILs are polyelectrolytes with monomer units of typical ionic liquids, thus combining attractive IL properties (wide electrochemical windows, thermal and chemical stability, low vapor pressure, non-flammability and non-volatility properties) with polymer features (i.e., mechanical robustness, particularly durability, low toxicity, and rapid manipulation via classical polymer processing methods).[6,7] PILs also have an exceptional capacity to modify the corresponding ions to easily control the physico-chemical properties of the polymers.[8–10] Therefore, it is possible to manufacture them using a variety of 3D methods, including inkjet printing,[11] digital light processing (DLP),[2,12] and masked stereolithography (MSLA).[13]

In the last decade, antibiotic resistance has emerged as a worldwide concern.[14,15] To overcome this issue, new materials with inherent antimicrobial activity are being developed.[16] In particular, polymeric matrices have recently attracted a lot of interest due to their higher efficiency, lower toxicity, minimization of environmental problems, resistance, and extended lifetime compared to their small molecular counterparts.[17] In addition, there are many antimicrobial agents that can be added as fillers into the polymeric matrices, such as metallic nanoparticles (NPs).[18–21] However, a challenge that might arise when working with NPs is their effective stabilization. Different strategies employing 3D printable polymers have been proven effective to offset this issue.[22] In this regard, due to their ionic and supramolecular interactions, PILs are excellent matrices for stabilizing molecular and nanostructured materials.[23,24] The employment of PILs for antimicrobial applications has grown in popularity during the past 5 years. Imidazolium-based PILs often receive the greatest research attention because of their exceptional thermal stability, low glass transition temperatures (Tg) values, and simplicity of synthesis.[25] The antimicrobial activity of imidazolium salts and their polymer derivatives is now well known,[10,26–28] and in contrast to the cytotoxic ILs, PILs have shown to be biocompatible.[29–33] Brushes with strong antibacterial activity based on imidazolium PILs have been successfully printed.[34] Apart from imidazolium groups, cholinium-based PILs have showed some antimicrobial activity as well.[35] Despite these encouraging results, the combination of PIL formulations with antimicrobial activity and 3D printing is still in its early stages.[36] The inherent ability of PILs to stabilize and support metal precursor salts and NPs throughout the printing process has been extensively documented. Wales et al. has demonstrated the possibility to 3D print PIL-based materials with silver salts, controlling the synthesis and stabilization of silver nanoparticles (AgNPs). The formation of AgNPs was effectively decoupled from the manufacturing process, and the printed films outperformed pure PILs in terms of antibacterial activity.[37]

Nevertheless, safety concerns have been raised over the usage of AgNPs because they pose potential hazards and can accumulate in the environment. *In vivo* tests demonstrated that the exposure of sublethal doses reduced animal and young adult lifespan and weakened their resistance to oxidative stress.[38] The substitution of silver salts for copper salts is of great interest for improving the sustainability and biocompatibility of the process and the devices.[39] The natural antimicrobial activity of copper (Cu), copper oxide (CuO), and copper alloys are well established,[40–42] and they have been used in a variety of applications

such as clinical ones, food packaging, and textiles.[43,44] The addition of Cu NPs to 3D-printable polymers can be beneficial for developing medical devices, enhancing the antimicrobial properties, and avoiding bacterial growth.[45–49] Muwaffak et al. incorporated metallic copper into an FDA-approved polymer (polycaprolactone) to produce filaments for 3D printing. In that way, customized wound dressings were prepared. However, high temperatures were required in the printing process.[50] In the literature, there are few examples of antibacterial materials mixing PILs with copper as antimicrobial agent, despite demonstrating low hemolysis against human cells and high long-term antibacterial stability.[51] The effective encapsulation of the copper-based compounds and nanomaterials is also an effective strategy to minimize their release to the environment, avoiding eco- and cytotoxicity concerns on the environment and human health.[52–54]

In our previous work, we demonstrated high antimicrobial activity using Ag@PIL composites[37]; however, the reported formulations also possessed high cytotoxicity, leaving room for development to mitigate this aspect. Within this context, our aim was to develop bespoke formulations for additive manufacturing that maintained antimicrobial activity but possessed reduced cytotoxicity. Here, we report a broad variety of novel 3D-printable formulations that were fully characterized and optimized to be manufactured by DLP and MSLA with the desired geometries at high resolution. Then, the optimum formulations were functionalized with Cu NPs. The materials demonstrated bactericidal activity against a model skin bacterium *Staphylococcus epidermidis*. This novel Cu@PIL formulation was used for successfully 3D-printing a medical demonstrator.

RESULTS AND DISCUSSION

In this work, biocompatible PILs based on a mixture of monomeric ionic liquid (mIL) with a cross-linker and a photoinitiator (PI) were prepared. In this regard, a variety of mILs and PIs were combined and evaluated. The three mILs tested were 1-butyl-3-vinylimidazolium bis(trifluoromethane)sulfonimide (mIL1), 1-(3-hydroxy propyl)-3-vinylimidazolium bis(trifluoromethane)sulfonimide (mIL2) and [2-(acryloyloxy)ethyl] trimethyl-ammonium bis(trifluoromethylsulfonyl)imide (mIL3), represented in Figure 1. Both mIL1 and mIL2 were synthesized from their bromide salt via anion metathesis as described in the electronic supplementary information (ESI). Then, mIL3 was synthesized from commercial [2-(acryloyloxy)ethyl]trimethyl-ammonium chloride ([AcrEMA][Cl]) by anion exchange, also described in the ESI. Polyethylene glycol diacrylate (PEGDA) monomers with different average molecular weights (250, 575, 700 g/mol) were employed as cross-linker. These can influence kinetics of polymerization, mechanical properties, and ultimately printing precision. Lastly, the photoinitiators studied were phenylbis(2,4,6-trimethylbenzoyl)phosphine oxide (BAPO), diphenyl(2,4,6-trimethylbenzoyl)phosphine oxide (TPO), and 2,2-dimethoxy-2-phenylacetophenone (DPAP). All the tested formulations are summarized in Table 1.

The polymeric formulations were optimized in order to obtain printings with high resolution. A wide variety of photopolymers were prepared and characterized using the three monomeric
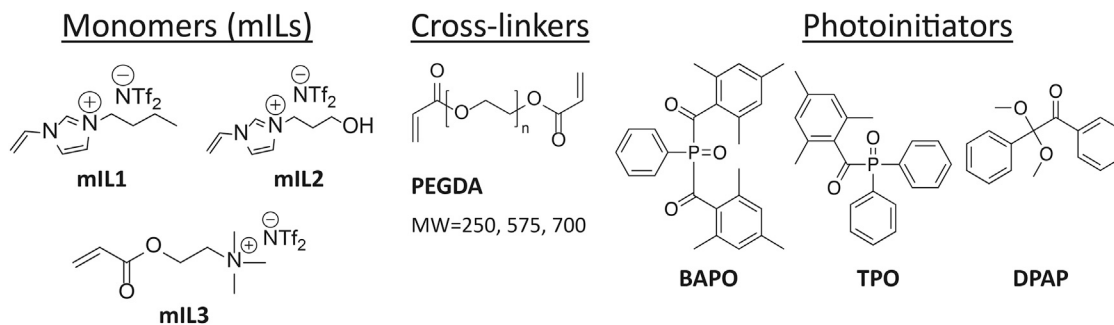
Figure 1. Main components evaluated for developing 3D-printable biocompatible and antimicrobial formulations

ionic liquids. The range of concentrations of mIL:PEGDA were varied from 100:0 to 60:40, while BAPO concentration was fixed at 1 wt % (Table 1). Furthermore, a low concentration of a dye was added to improve the resolution. In this way, methyl red was added (0.1 wt %), giving a distinctive red color on all the printings.

Important parameters such as polymerization kinetics were analyzed to get good printing conditions. Polymerization kinetics of all the formulations were followed by photorheology. Once the storage modulus reached a plateau, the polymerization was completed. As it can be seen in Figure 2A, mIL3.2 reactivity (black line) was faster than that of mIL2.2 (red line) and mIL1.2 (blue line) due to its acrylate double bond. The reactivity of mIL3.2 was similar to that of the diacrylate groups of PEGDA (green line). In contrast, imidazolium-based formulations, mIL2.2 and mIL1.2, had a vinyl double bond that was slightly slower to initiate polymerization, as can be seen from the delay time. The delay time before starting the photopolymerization for mIL3.2 was around 0.3 s, while for mIL2.2 and mIL1.2, it was more than 2 s. The storage modulus was similar between them, reaching a plateau around 10^5 Pa, which means that the polymerization was completed at that point. However, great differences were found when measuring the monomeric formulations without cross-linker (mIL1.4, mIL2.4, mIL3.4), which presented higher delay times and much slower kinetics (related with the slope gradient) (Figure S1). This behavior was expected since pure mIL formulations are less reactive, requiring longer time and more energy to polymerize. Indeed, the mILs without cross-linker were unable to manufacture solid 3D objects because the polymerization was only partial, and the polymeric conversion and the gel content of the films are shown in Table 1.

The polymerization reactions were followed by Fourier transform infrared spectroscopy (FTIR), whereby the absence of C=C double bond vibrations at 1,640 cm^{-1} and 990 cm^{-1} was used to calculate the conversion (Figure 2B). To this end, the evolution of the FTIR signals belonging to the acrylate and vinyl functional groups before and after 3D-printing irradiation were analyzed. The polymeric conversion was calculated according to the literature.[55] The spectra were normalized using the area of the SO$_2$ band at 1,350 cm^{-1}, belonging to the counter-anion bis(trifluoromethane)sulfonimide. At the same time, the presence of unreacted monomers in printed flat samples was evaluated by extraction in chloroform, indicating the percentage of insoluble fraction for each sample (gel content).

The gel content and the polymeric conversion provided information on the reactivity and the degree of polymerization of each formulation. From Table 1, it can be concluded that, in general, mIL3 formulations polymerized more efficiently due to their highest reactivity. As it was expected, a larger molar percentage of cross-linker led to higher degrees of polymerization, with some exceptions. Thus, pure PIL formulations (PILx.4, Table 1, entries 5, 11, and 17) reported generally low gel content and polymeric conversion percentage. Table 1 also reveals that formulations using PEGDA 250 were less effective than those with PEGDA 575 and PEGDA 700.

Finally, dynamic mechanical thermal analysis (DMTA) was performed using printed flat films to evaluate the T_g of the polymers. The results are in good agreement with the theoretical values calculated with the Fox equation, even if some discrepancy seems to emerge, especially for formulations based on mIL3, which resulted in more flexibility than what we expected. On the other hand, it must be noted that the Fox equation is an empirical law, which does not take into consideration intermolecular interactions or variations of cross-linking density. At last, data for PIL2.5 sample are missing because this specimen demonstrated to be too fragile with tendency of crack formation, resulting in being not suitable for DMTA testing.

The printing parameters were adjusted for each formulation to improve the resolution of the printed parts (see Table S1). The main parameter modified was the exposure time per layer, which is related to the reactivity of each formulation. All the printing procedures are characterized by two different exposure times, one for the first layer and the other for the rest of the printing. Generally, in bottom-up configuration, the first printed layers (*burn-in layers*) need a longer light exposure time to ensure their attachment to the platform. Other parameters were modified to improve printing procedure, namely, the separation and approach velocities and the slides per layer. The compositions were processed with an Asiga PICO2 DLP printer to manufacture complex and bespoke macroscopic devices, with tailored shapes and properties. By varying the ionic monomer concentration, the molecular weight of the cross-linker and the display images, precise 3D design, and specific polymeric properties were achieved.

All the printings were scanned by a 3D scanner to evaluate the fidelity of the printed part to the digital design (Figures 2C–2E). That equipment reported the resolution of the printings after comparing the scanned figures with the original CAD models.

Table 1. Summary of all the formulations prepared and a quantitative assessment of the properties of the materials developed

| mIL	Code	mIL (mol %)	PEGDA (MW)	PEGDA (mol %)	Conversion (%)	Gel content (%)	T_g (°C)	Theoretical T_g (°C)[a]
N/A	PEGDA	0	250	100	90	99	30	N/A
N/A	PEGDA	0	575	100	99	99	−20	N/A
N/A	PEGDA	0	700	100	99	99	−30	N/A
mIL1	PIL1.1	60	575	40	98	81	−10	−17.9
	PIL1.2	80	575	20	99	71	−14	−17.1
	PIL1.3	90	575	10	99	57	−14	−16.7
	PIL1.4	100	N/A	0	62	50	−16	N/A
	PIL1.5	80	250	20	97	68	−4	−8.2
	PIL1.6	80	700	20	99	74	−27	−19.2
mIL2	PIL2.1	60	575	40	90	90	−10	−2.6
	PIL2.2	80	575	20	96	95	1	3.7
	PIL2.3	90	575	10	35	93	7	7.1
	PIL2.4	100	N/A	0	48	89	10	N/A
	PIL2.5	80	250	20	75	67	N/A	N/A
	PIL2.6	80	700	20	76	82	−3	1.4
mIL3	PIL3.1	60	575	40	98	99	6	24.4
	PIL3.2	80	575	20	93	99	24	42.9
	PIL3.3	90	575	10	98	98	57	53.1
	PIL3.4	100	N/A	0	73	90	64	N/A
	PIL3.5	80	250	20	63	93	7	56.6
	PIL3.6	80	700	20	99	95	2	40.8

[a]Calculated applying the Fox equation.

Both mIL3 and mIL2 formulations could be printed with similar parameters, although their composition was different, since mIL3 was a cholinium monomer and mIL2 was an imidazolium, while the other imidazolium monomer, mIL1, needed much more time and slides per layer in order to obtain good printings. Still, the resolution of both imidazole monomers was remarkably lower (with a standard deviation [σ] between the scan data and the reference model of 0.37 mm), probably due to the inferior reactivity of the vinyl groups of the imidazolium in contrast to the acrylates from the cholinium (σ = 0.20 mm).

Likewise, formulations with PEGDA 250 and PEGDA 700 were not suitable for printing elaborate devices, and only flat bases were properly printed. The parts were either too tightly cross-linked or not enough, in both cases resulting in some deformation in the complex structures. For that reason, PEGDA 575 was chosen as the cross-linker in future tests. Additionally, the printing resolution of formulations with 90 mol % of mIL was in general poor (σ ∼ 0.45 mm). In contrast, formulations with 80 mol % of mIL presented printing accuracy (σ ∼ 0.25 mm) (Figure S2).

At this point, biological tests on the most promising formulation (80:20 mIL/PEGDA 575) were performed. In a previous work, the antibacterial films based on mIL2 (PIL2.2)[37] showed high cytotoxicity to a mammalian epithelial cell line (Figure S3). In that work, cell viability assays performed on Vero cells incubated with PIL2.2 were apoptotic, a form of programmed cell death, while the cells with Ag@PIL2.2 suffered necrosis, a form of traumatic cell death that results from acute cellular injury. In contrast, the viability of mIL1 and mIL3 formulations (PIL1.2 and PIL3.2) was

notably superior. These preliminary operative studies demonstrate how the monomer affects biocompatibility of the derived PIL. Additionally, photoinitiators with low cytotoxicity were also crucial. Polymerized samples containing BAPO resulted in low cell viabilities, while films based on DPAP and TPO presented a high biocompatibility. As it can be seen in Figure 3, the same monomer (mIL1) was photopolymerized using the three PIs, showing generally lower cytotoxicity when using DPAP and TPO. Likewise, different concentrations of PI were tested (0.5 wt %, 1 wt %), finding improved cell viability with lower PI concentrations. Therefore, both components, mILs and PIs, played an important role for reaching biocompatible PIL-based formulations. Moreover, a thorough washing protocol was applied to remove the unreacted and potentially cytotoxic products (monomers and photoinitiator) from the material. This is important to avoid misleading results in the biocompatibility tests. The washing step consisted of immersing the samples in 70% ethanol for 1 h to remove unreacted monomers and excess PI before performing the cell viability tests. This washing step also served to sterilize the samples before performing these assays.

Hence, in the next studies, the formulations evaluated contained the monomers mIL1 or mIL3 using TPO as photoinitiator with the concentration fixed at 0.5 wt %. Differently from previous work, a copper salt was added to the monomeric mixture to obtain antimicrobial devices. The first test performed aimed at assessing if the presence of these salts may affect kinetics of photopolymerization, by means of photorheology experiments. This investigation evidenced that the presence of salts did not affect photocuring behavior since reaction time and
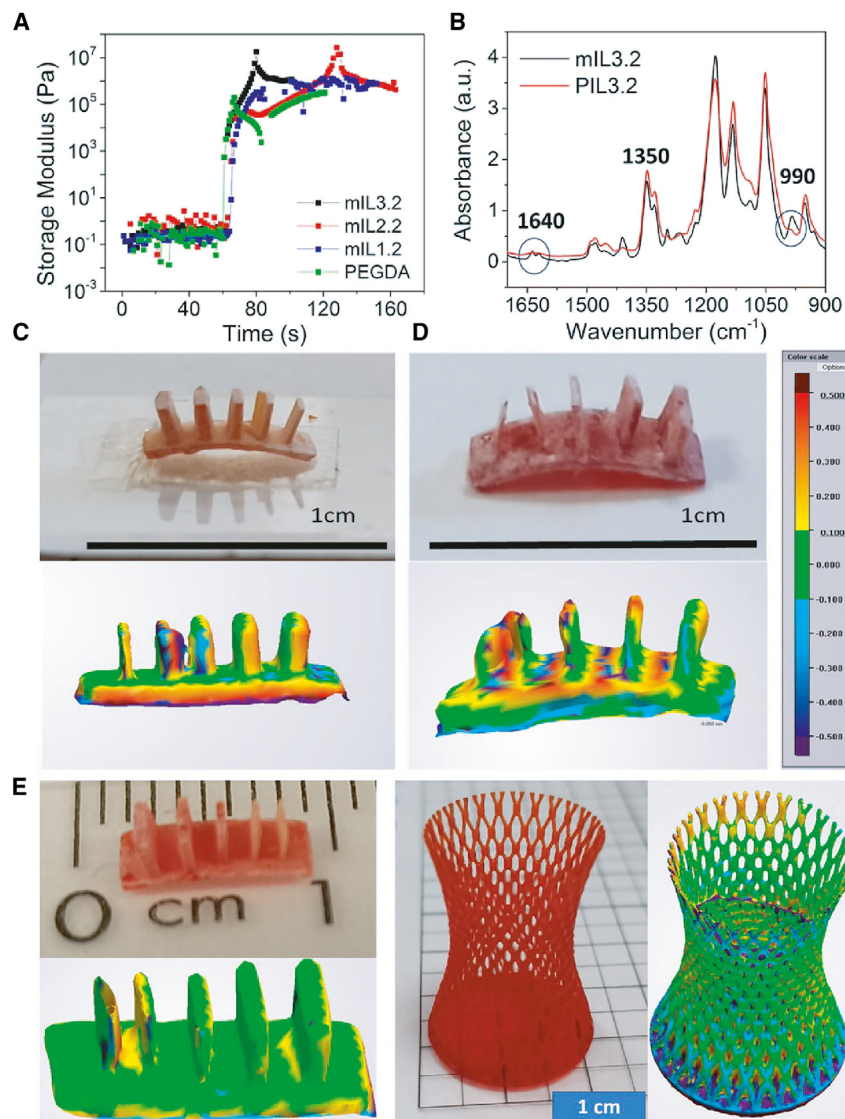
Figure 2. Printability of the mIL-based formulations

(A) Photorheology curves of the three monomers with PEGDA 575 (mIL1.2, mIL2.2, mIL3.2) compared with pure PEGDA 575 (PEGDA).

(B) FTIR spectra before 3D-printing (mIL3.2) and after (PIL3.2), showing the disappearance of the C=C peaks (at 1,640 and 990 cm^{-1}), while the reference peak (1,350 cm^{-1}) kept constant; 3D-printed structures using different formulations.

(C) PIL1.2.

(D) PIL2.2.

(E) PIL3.2 and the evaluation of the printing resolution by comparing the STL file to the scanned image acquired from the printed parts. The highest resolution achieved was 50 μm.

rate were similar, and all the curves reached a similar modulus plateau at the end of the process (Figure 4).

UV-vis spectra of the polymerized film containing Cu species (Figure S4A) showed the characteristic band of the copper, evidencing proper dispersion.[56] Different concentrations of copper salt (1 and 2 wt %) were tested (Figure S4B). As expected, the copper band was significantly more evident using 2 wt %. Furthermore, copper presents less bactericidal effect than silver,[41] so we decided to use 2 wt % of copper concentration in the following tests.

The chemical oxidation state of copper in the films was further investigated by characterization with X-ray photoelectron spectroscopy (XPS). Figure 5 exhibits the high-resolution XPS Cu 2p and Cu LMM Auger spectra of the Cu@PIL1.2 film, where a doublet located at ~932/952 eV was obtained. However, the typical satellite of Cu(II), around 942–944 eV, was not identified. The doublet identified is characteristic of Cu(OH)$_3$NO$_3$ species,[57]

while it does not appear in the XPS of Cu(NO$_3$)$_2$ found in the literature.[58] The spectra were calibrated using the energy reference of the C 1s (C–C) at 285 eV.

So, the copper in PIL1.2 film could be a mixture of Cu(I) and Cu(II), explaining the absence of Cu(II) satellites. According to similar XPS results found in the literature, copper (I) could form a complex with the C2 of the imidazolium group.[59–61] Still, the copper contained in our films seemed to be reactive and unstable, indicating a mixture of copper species. This factor made it difficult to identify the copper state by FTIR and Raman spectroscopy, where we could not identify any characteristic band (Figure S5). The PIL-based formulation may not be the strongest or most appropriate stabilizing system for the copper species formed. The formation of Cu NPs usually requires reducing and stabilizing agents to generate Cu(I) and Cu(0) species. Furthermore, these species are often oxidized to CuO.[62] Alternatively, a hydrolysis of the Cu precursors to generate Cu(OH)$_2$ and Cu$_2$(OH)$_3$NO$_3$ followed by a thermal treatment generates CuO NPs.[63] In some cases, a thermal decomposition of Cu(II) precursors into NPs has been reported.[64] The presence of polyethylene glycol and derivatives has proven to facilitate the formation of CuO NPs.[65] In our case, we treated our copper samples at 160°C for 30 min (Cu@PIL1.2-h), finding that the color of the films changed progressively from green to dark brown (Figure S6A). Furthermore, there seems to be an increase in the absorption below 400 nm, which could be attributed to CuO NPs.[62] Whereas, neither our pristine formulation PIL1.2 nor pure Cu(NO$_3$)$_2$·3H$_2$O changed their color to dark brown after heating. This indicates that a reaction of the copper species occurred within the PIL. This color change is consistent with the formation of CuO NPs.[66] Pure Cu NPs are more likely to produce a strong absorbance in the NIR region (ca. 500–1,200 nm, depending on their size and shape) due to a strong localized surface plasmon of resonance.[67] However, XPS analysis was
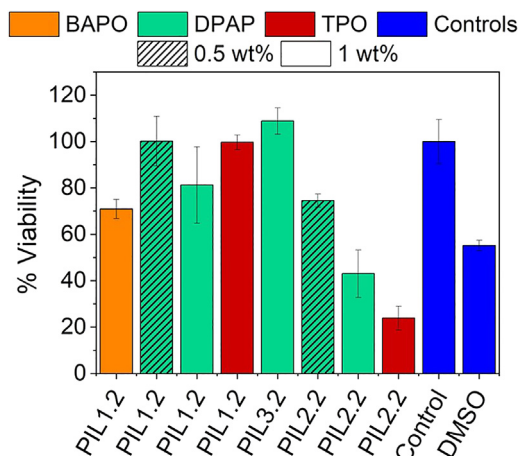
Figure 3. Cell viability test using different formulations, changing the monomers (mIL1, mIL2, mIL3), the PI, and the weight percentage of PIs

The control of the experiment was carried out using a highly biocompatible sample (control) and dimethyl sulfoxide (DMSO) (blue) as a reference of a toxic environment for cells. All formulations were prepared using mIL (80 mol %) and PEGDA 575 (20 mol %). Error bars represent the standard deviation of four replicas.

Figure 4. Photorheology spectra of mIL1.2 formulation (black) and same formulation with silver (red) and copper (blue)

inconclusive since copper signals were not detected after heating (Table S2). Copper species may have migrated from the surface to the core of the sample due to a possible encapsulation effect of the monomer after the thermal treatment, becoming undetectable by XPS. In both samples, C 1s has the same chemical species; however the intensity of **C**–N/**C**–O and (C=O)-**O**-C/**C**–S species is evidently different; this could be consistent with a change of surface groups after the thermal treatment. UV-vis analysis was performed after heating the samples at different temperatures. In Figure S6B can be seen the absorption peak features for the CuO (at 430 nm) in the sample heated at 100°C (blue spectrum). In the rest of the samples, that band was not so visible, since the absorption of species in the UV region seems to saturate the signal observed. The more heated the films were, the more yellowish/brownish they appeared (Figure S6C). That must be the reason why the signal started to be saturated around 450 nm, where compounds with yellow color absorb. The film heated at 100°C presented lower absorption, and thus, the signal was less saturated. In this case, a convoluted band attributed to CuO was observed. Thinner films could avoid saturation, but it was not possible to prepare such films by 3D printing. In addition, the characteristic signal of CuO is a band of low absorption.[68] After heating the samples for 30 min at 160°C, the resulting copper species seemed better stabilized than untreated samples, probably due to the formation of Cu NPs, which was confirmed by transmission electron microscopy (Figure S7). The materials were characterized by XRD (Figure S8) to confirm the composition of the NPs, but unfortunately due to their low concentration and the effect of the polymeric matrix, no positive results were obtained. Further attempts to characterize the nature of the nanomaterials were attempted by heating PIL1.2 at 200°C and 240°C. Even though high-angle annular dark-field scanning transmission electron microscopy (HAADF-STEM) shows the presence of NPs
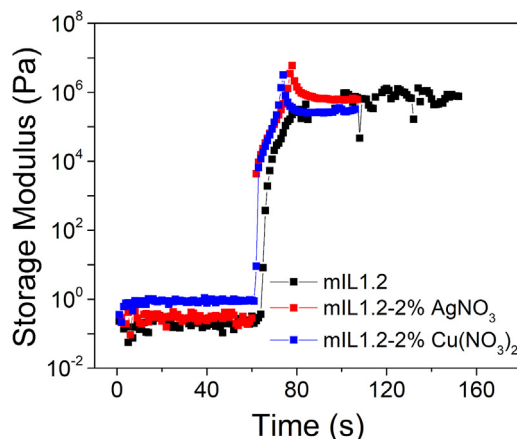
(Figure S9), again, it was not possible to characterize the exact nature of the nanomaterials. Dynamic mechanical analysis measures viscoelastic properties of materials, giving conservative modulus (E′), loss modulus (E''), and their ratio (tan delta), and its maximum is used to define T_g of the polymeric materials. The analyses showed a stiffening of the polymer upon the addition of Cu and the thermal treatment to form the NPs, evidenced by an increase in the ratio of the loss modulus (E'') to the storage modulus (E′), i.e., tan delta of ca. 20°C in the presence of the copper species, while E′ modulus increased from 9 MPa for the polymeric materials to 15 MPa for the nanocomposite at room temperature (Figure S10). This means that the materials are losing elasticity upon the formation of nanomaterials in their matrix. This is in good agreement with previous results obtained with AgNPs, where the presence of NPs resulted in a stiffening of the polymeric supports.[37] In summary, the addition of copper salts in the PIL matrix followed by a controlled thermal treatment generated NPs. Even though the changes in color and UV-vis spectra are consistent with the formation of CuO NPs,[66] the exact nature of the oxidation state and nature of the NPs remains elusive, where possibly Cu or CuO species and their exact characterization will be the focus of future work.

As a proof of concept, a part with a geometry compatible with a medical stent was 3D-printed using our customized photopolymers (Figure 6A). The stent was manufactured using a formulation based on PIL3.2, obtaining high printing resolution using an MSLA printer. The stent was properly printed with and without copper. The microscopic images obtained for the different stents show the impressive detail of the printings, smaller than 200 μm (Figure 6B). Moreover, it was possible to print a Cu@PIL3.2 stent with the size halved at very high precision, with an error <5% (calculated from the difference in the main dimensions set in the CAD file compared to optical microscopic images of the printed part) (Figure 6C).

The heating treatment (30 min at 160°C) did not affect the printed part; thus, it was possible to obtain highly resolved stent-like geometries with NPs of copper without affecting the structure (Figures S11A and S11B). In contrast, the formulation based on mIL1.2 with copper was not able to build this complex
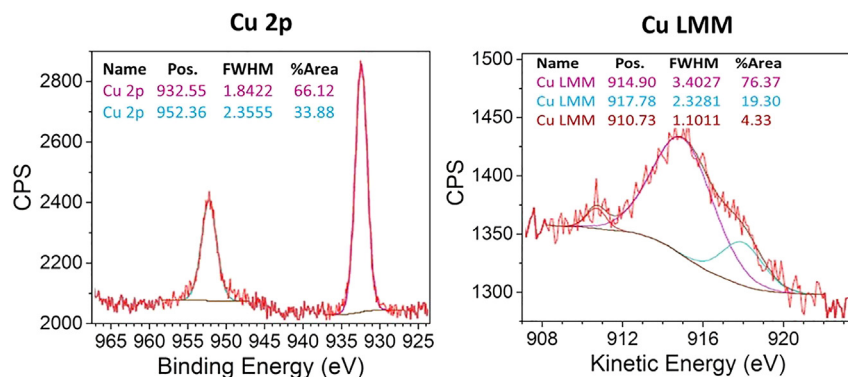
Cu 2p

Name	Pos.	FWHM	%Area
Cu 2p	932.55	1.8422	66.12
Cu 2p	952.36	2.3555	33.88

Cu LMM

Name	Pos.	FWHM	%Area
Cu LMM	914.90	3.4027	76.37
Cu LMM	917.78	2.3281	19.30
Cu LMM	910.73	1.1011	4.33

Figure 5. High-resolution XPS of Cu 2p and Cu LMM Auger spectra for Cu@PIL1.2 sample

stent structure. As can be seen in Figure S11C, only the supporting base of the object was properly printed. Consequently, this material formulation can be considered suitable only for coarser structures (dimension of the struts >250 μm). The long-term stability of the materials and printed structures was not specifically studied, but it was observed that the PILs remain stable over time; i.e., they retain their structural integrity and do not become brittle and fall apart for several years. Old samples (with known antibacterial activity) were employed as internal controls when evaluating the activity of new batches of materials. Related PIL-based materials have been recently employed to stabilize highly sensitive perovskite nanocrystals, and their properties were maintained over extended periods of time.[69]

Finally, the antimicrobial activity of the copper samples was evaluated, which changed with the heating treatment. Unfortunately, despite having high cell viability, PIL3.2 films were found to have poor antimicrobial activity. For that reason, the antimicrobial analysis was focused on Cu@PIL1.2 films, since PIL1.2 formulation had reported high biocompatibility and antimicrobial activity in previous studies.[37] The bactericidal properties of the copper-based films before (Cu@PIL1.2) and after thermal treatment at 160°C (Cu@PIL1.2-h) were studied against *S. epidermidis* in order to exploit the biocompatibility of the PIL materials for medical devices. In our study, Cu@PIL1.2-h samples produced a 98% bacterial cell reduction in liquid media (Figure 7). These results correlate with the ones obtained by similar systems, such as Zheng et al., whose PIL membranes containing copper resulted in a 99% decrease in bacterial cell viability.[51] In another study, Luo et al. developed PIL/Ce membranes with good hemocompatibility and cytocompatibility that were also able to reduce viable bacterial colonies after 4 h.[70] In contrast, Cu@PIL1.2 presented a degree of inhibition of around 70% with higher variability in the results. The higher antibacterial activity of Cu@PIL1.2-h could be explained by the rearrangement of the copper after being treated at 160°C. In this instance, the thermal treatment of the PIL probably promotes the formation of Cu NPs and makes the film more antibacterial.

Conclusions

The main objective of this work was to prepare non-toxic materials capable to be 3D-printed with high resolution by DLP and MSLA. The photopolymer's composition as well as the printing parameters were modified to obtain 3D printed parts with an improved accuracy that was evaluated by a 3D scanner. The effect of the monomeric ionic liquid and the photoinitiator employed was evaluated, finding that they both play an important role in obtaining biocompatible formulations.

Three different mILs were tested: 1-butyl-3-vinylimidazolium bis(trifluorome-thane)sulfonimide (mIL1), 1-(3-hydroxy propyl)-3-vinylimidazolium bis(trifluorome-thane)sulfonimide (mIL2), and [2-(acryloyloxy)ethyl]trimethyl-ammonium bi(trifluoro-methylsulfonyl)imide (mIL3). While mIL1 and mIL3 had low toxicity, mIL2 was extremely toxic. Likewise, formulations using BAPO were very toxic compared to those using DPAP and TPO. In addition to choosing appropriate materials, a proper post-printing technique was necessary for developing non-toxic materials. In order to increase the antimicrobial activity, copper salts were successfully encapsulated in PILs (Cu@PILs), taking advantage of their ability to stabilize and support metal precursor salts and NPs. Even if the exact nature of the nanomaterials could not be determined, the synthesis of the materials, their printability, and antimicrobial activity were found to be reproducible.

A treatment based on heating the photopolymerized samples at 160°C was necessary to form Cu NPs and to enhance the stabilization of the metal in the films. These functional formulations were evaluated to 3D-print a medical demonstrator. In particular, very high resolution was proved for formulations based on mIL3, which in turn did not show antimicrobial properties. On the other hand, formulations based on mIL1 showed lower resolution but excellent bactericidal characteristics. The antimicrobial activity of the copper-based films was investigated for both the treated and non-treated samples, finding a higher activity for the former ones. In particular, the heated films exhibited remarkable potential to inhibit the growth of *S. epidermidis* bacteria (98%).

In summary, this research demonstrates that high-resolved devices can be obtained by additive manufacturing. Furthermore, the formulations used constitute a breakthrough in the preparation of solid antibacterial materials with desired characteristics and specific requirements such as biocompatibility. The functional materials prepared in this study have a potential interest for antimicrobial applications.

EXPERIMENTAL PROCEDURES

Resource availability

Lead contact

Further information and requests for resources should be directed to and will be fulfilled by the lead contact, V. Sans (sans@uji.es).
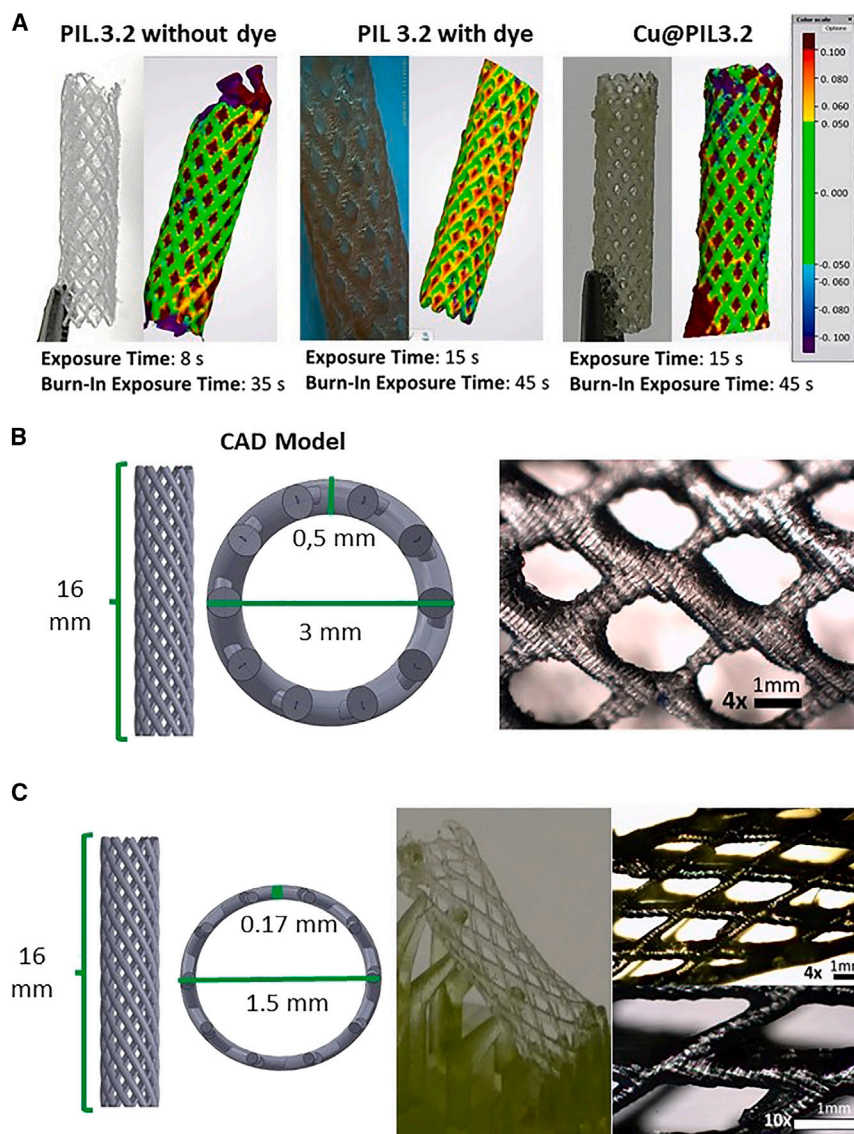
Materials availability

The polymeric formulation generated here is available and can be requested from the lead contact upon reasonable request.

Data and code availability

Any additional information required to reanalyze the data reported in this paper is available from the lead contact upon request.

(A) Comparison of the printability of the printed devices: optical images and resolution analyses with 3D scanner of stents printed from PIL3.2 with and without dye and with Cu.
(B) CAD model of a "thick" stent and optical image of the detail of the printed features of Cu@PIL3.2.
(C) CAD model of a "thinner" stent before and after the thermal treatment.

ware used to create slices was Asiga Composer. For the Elegoo Mars 2 Pro 3D printer, the slicer software employed was ChituBox.

The software for additive manufacturing allowed us to define a desired thickness (100 μm per layer), to manage the projector's projection time, and to regulate the build plate's movement speed. The build plate was then dropped into the mixture at the bottom of the printer vat, which had been previously filled with the different formulations. At this stage, the program directed the projector to show white pictures of each of the layers that needed to be photocured against a black background. The translucent bottom of the vat allowed the UV light to penetrate through. Each layer was cured for 8 s. After that time, the printer showed a black background while the build plate was automatically lifted by 70 μm at a predetermined speed. This methodology was followed for each layer until the object was completed. After manufacturing, the device was removed and thoroughly cleaned with isopropyl alcohol to eliminate any uncured ink. Finally, the part was photocured under UV light at 40°C for 20 min.

Photorheology

Real-time rheological measurements were performed using an Anton Paar rheometer (Physica MCR 302) in parallel plate mode with a Hamamatsu LC8 lamp with visible bulb and a cutoff filter below 400 nm equipped with 8-mm light guide. The distance between the two plates was fixed to 0.2 mm. The sample was kept at an established temperature (25°C) and shear frequency (1 rad s^{-1}). In order to allow the system to stabilize, the visible light was switched on after 60 s. Concomitant changes in viscoelastic material moduli during polymerization were measured as a function of exposure time.

Synthesis of ionic liquids

Full synthesis details and characterization data are given at the end of the ESI (Figures S12–S19).

### Preparation of photocurable formulations containing copper salt

In a typical procedure, the main printable formulation was prepared by mixing 80 mol % mIL1 or mIL3, 20 mol % PEGDA 575, considering the MW of the monomer, 0.5 wt % TPO, and 2 wt % copper dinitrate (Cu(NO$_3$)$_2$·3H$_2$O), with respect to the total mixture (80:20 mIL:PEGDA). Additionally, formulations without copper precursor were prepared as references. For the optimization process, various formulations have also been tested, and a complete list can be observed in Table 1.

Process for 3D printing PIL networks

The procedure for 3D printing monomeric ionic liquids was the same for all formulations. The CAD files were designed and converted to STL-type files using SolidWorks CAD software. The DLP fabrication in both printers began by slicing the 3D CAD model into individual 2D images for projecting onto the photocurable liquid. For the Asiga PICO printer, the additive manufacturing soft-

Fourier transform infrared spectroscopy

The spectrometer used was a Nicolet iS50 FTIR from Thermo Fisher Scientific, equipped with an attenuated total reflection accessory (Smart iTX, Thermo Fisher Scientific). This apparatus was used to study the final conversion and reactivity of the different formulations after the polymerization process. To this end, the evolution of the FTIR signals belonging to the acrylate and vinyl functional groups before and after irradiation with ultraviolet light was analyzed. The polymeric conversion was calculated according to the literature.[55] The spectra were normalized using the area of the carbonyl ester band at 1,350 cm^{-1}. The disappearance of the bands related to the C=C bond at 1,640 and 990 cm^{-1} verified the conversion of the double bonds after polymerization. The spectra were recorded with a resolution of 4 cm^{-1} in the wavelength range between 650 and 4,000 cm^{-1} averaging 16 scans for each spectrum.
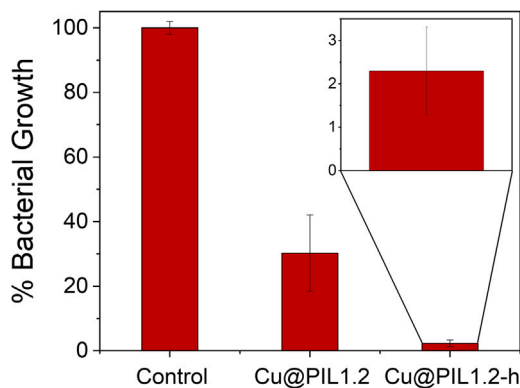
Figure 7. Bacterial cell growth of *S. epidermidis* incubated with Cu@PIL1.2 and Cu@PIL1.2-h vs. the control experiment. Error bars repesent the standard deviation of six replicas.

Gel content

The insoluble fraction (gel content) of polymerized samples was measured using the standard test method ASTM D2765-16.[71] Thin films (0.3–0.6 mm) were printed and placed in a metal net, previously weighed, and then soaked in chloroform at room temperature for 24 h to dissolve the non-crosslinked products. The samples were then dried overnight at 80°C, and the gel content percentage was calculated as the weight change before and after the solvent extraction.

Dynamic mechanical thermal analysis

The mechanical analyses were performed using a Tritec 2000 dynamometer (Triton 6 Technology, London UK), varying the temperature from −70°C to 80°C. The moduli measurements as a function of temperature were measured using a strain amplitude of 0.1% and frequency of 1 Hz. Printed flat films (30 mm × 10 mm × 0.5 mm) were prepared, and three replicates for each composition were tested. The T_g was measured as the temperature corresponding to the maximum of the tanδ curve (Figure S20).

3D scanner

The samples were scanned by a 3D optical scanner, 3Shape E3, to compare the printed parts with the CAD models. Then, 3Shape Convice Analyzer was used for performing the comparative analysis between them (accuracy 0.007 mm, ISO 12836). Before analyzing deviations, the scan data and the reference model must be aligned. In this work, the alignment was done using the "best fit" approach, which employs the least squares principle; i.e., the differences between the scan and the models are mathematically divided. The comparative analysis is shown as a heatmap.

Antimicrobial studies

All tested samples were 3D-printed with the same size (circles of 5 mm in diameter and 0.5 mm of thickness and squares 2 × 2 cm and 0.5 mm of thickness) to improve the reproducibility of the tests. Each sample was tested a minimum of three times (on separate days) to verify reproducibility.

The bacteria strain used, *Staphylococcus epidermidis* NCIMB 8853 CECT 231, was acquired from the Colección Española de Cultivos Tipo (CECT) as lyophilized bacteria. The bacteria cell bank suspensions were thawed and inoculated on a nutrient broth agar plate and on liquid nutrient broth for 24 h at 37°C with mild agitation. A first subculture was performed to assure viability of the strain. A dilution from these culture solutions (second subculture and so on) was used for the following tests, corresponding to an inoculum of 1×10^7 colony-forming units (CFU)/mL.

Bacterial cell proliferation assay

Bacterial growth was recorded measuring the optical density (OD) of the samples at 600 nm over a 24-h period using a microplate reader (Thermo

Scientific MULTISKAN GO). Results were compared with the OD variation of a control culture containing only *S. epidermidis*. Each experiment was repeated a minimum of three times to ensure that the results remained reliable across different inoculations. The data for all control experiments and antibacterial assays are based on a total of six repeats to confirm the reproducibility of the results and to calculate the mean values and the standard deviation. The PIL samples, previously sterilized with ethanol 70%, were placed in a 24-well plate inoculated with 1 mL of the inoculum (1×10^7 CFU /mL of *S. epidermidis*), incubated at 37°C with mild shaking, and the antiproliferative effects induced by the samples were observed by plotting OD vs. time. Bacterial growth was recorded measuring the OD of 100 μL collected from each well of the 24-well plate in a 96-well plate. Using a microplate reader, measurements were taken at 600 nm every hour for the first 8 h and then at 24 h as an endpoint. During the experiment, the 100 μL taken out of the wells of the 24-well plate was replaced with 100 μL of medium in order to maintain the final volume (1 mL). Results were compared with the OD variation of the positive control culture containing only bacteria (1 mL 10^7 CFU/mL of *S. epidermidis*). The negative control contained 1 mL of liquid media and served as baseline.

Cell cytotoxicity assays

The cytotoxicity of PIL-based materials was evaluated using a colorimetric assay based on the use of 3-(4,5-dimethylthiazolyl-2)-2,5-diphenyltetrazolium bromide (MTT). Vero cell lines, derived from African green monkey kidney tissue, were used to conduct the assay. They were grown (10,000 cells/well, 200 μL/well) on 96-well plates in DMEM culture medium 2 days before the experiment. The addition of the solid samples to cells would have resulted in a false result of high toxicity caused by cell compression. For this reason, samples were treated as follows.

PIL-based materials were weighed, sterilized with ethanol (70%), and rinsed with sterile distilled water before drying with filter paper. Each sample was then incubated in another 96-well plate, containing 200 μL of DMEM culture media, with phenol red for 24 h at 37°C, 5% CO_2.

On day 2, PIL-based materials were removed from the plate using tweezers, and they were dried and weighed. Cells were washed with PBS and exposed to the 200 μL of DMEM that had been incubated with PIL-based materials, while the positive controls received fresh DMEM. Then, cells were incubated for an additional 24 h at 37°C, 5% CO_2. On day 3, the cells were washed with PBS, and 200 μL of 0.5 mg/mL of MTT was added to each well and incubated for 1.5 h at 37°C, 5% CO_2. The supernatant was removed by centrifugation (2,500 rpm, 10 min), the formed formazan crystals were dissolved with 200 μL DMSO, and the color intensity was determined by photometric measurements at 570 nm after 10 min of stirring, and the cell viability was determined by comparing the absorbance data of each sample with the control samples (100% viability). Two independent experiments were performed, each with four parallel measurements.

AUTHOR CONTRIBUTIONS

DECLARATION OF INTERESTS

REFERENCES

1. Salas, A., Zanatta, M., Sans, V., and Roppolo, I. (2023). Chemistry in light-induced 3D printing. ChemTexts *9*, 4.

2. Wales, D.J., Cao, Q., Kastner, K., Karjalainen, E., Newton, G.N., and Sans, V. (2018). 3D-Printable Photochromic Molecular Materials for Reversible Information Storage. Adv. Mater. *30*, 1800159.

3. Ngo, T.D., Kashani, A., Imbalzano, G., Nguyen, K.T., and Hui, D. (2018). Additive manufacturing (3D printing): A review of materials, methods, applications and challenges. Compos. B Eng. *143*, 172–196.

4. Emon, M.O.F., Alkadi, F., Philip, D.G., Kim, D.-H., Lee, K.-C., and Choi, J.-W. (2019). Multi-material 3D printing of a soft pressure sensor. Addit. Manuf. *28*, 629–638.

5. Sevilla, S., Yong, M., Grinstein, D., Gottlieb, L., and Eichen, Y. (2019). Novel, Printable Energetic Polymers. Macromol. Mater. Eng. *304*.

6. Nishimura, N., and Ohno, H. (2014). 15th anniversary of polymerised ionic liquids. Polymer *55*, 3289–3297.

7. Sans, V., Karbass, N., Burguete, M.I., Compañ, V., García-Verdugo, E., Luis, S.V., and Pawlak, M. (2011). Polymer-supported ionic-liquid-like phases (SILLPs): transferring ionic liquid properties to polymeric matrices. Chemistry *17*, 1894–1906.

8. Mecerreyes, D. (2011). Polymeric ionic liquids: Broadening the properties and applications of polyelectrolytes. Prog. Polym. Sci. *36*, 1629–1648.

9. Sengupta, A., Kumar Ethirajan, S., Kamaz, M., Jebur, M., and Wickramasinghe, R. (2019). Synthesis and characterization of antibacterial poly ionic liquid membranes with tunable performance. Separ. Purif. Technol. *212*, 307–315.

10. Zheng, Z., Xu, Q., Guo, J., Qin, J., Mao, H., Wang, B., and Yan, F. (2016). Structure–Antibacterial Activity Relationships of Imidazolium-Type Ionic Liquid Monomers, Poly(ionic liquids) and Poly(ionic liquid) Membranes: Effect of Alkyl Chain Length and Cations. ACS Appl. Mater. Interfaces *8*, 12684–12692.

11. Karjalainen, E., Wales, D.J., Gunasekera, D.H.A.T., Dupont, J., Licence, P., Wildman, R.D., and Sans, V. (2018). Tunable Ionic Control of Polymeric Films for Inkjet Based 3D Printing. ACS Sustain. Chem. Eng. *6*, 3984–3991.

12. Maciel, V.G., Wales, D.J., Seferin, M., and Sans, V. (2019). Environmental performance of 3D-Printing polymerisable ionic liquids. J. Clean. Prod. *214*, 29–40.

13. Schultz, A.R., Lambert, P.M., Chartrain, N.A., Ruohoniemi, D.M., Zhang, Z., Jangu, C., Zhang, M., Williams, C.B., and Long, T.E. (2014). 3D Printing

Phosphonium Ionic Liquid Networks with Mask Projection Microstereolithography. ACS Macro Lett. *3*, 1205–1209.

14. Wright, G.D. (2011). Molecular mechanisms of antibiotic resistance. Chem. Commun. *47*, 4055–4061.

15. Blair, J.M.A., Webber, M.A., Baylay, A.J., Ogbolu, D.O., and Piddock, L.J.V. (2015). Molecular mechanisms of antibiotic resistance. Nat. Rev. Microbiol. *13*, 42–51.

16. Jones, A., Mandal, A., and Sharma, S. (2015). Protein-based bioplastics and their antibacterial potential. J. Appl. Polym. Sci. *132*.

17. Jain, A., Duvvuri, L.S., Farah, S., Beyth, N., Domb, A.J., and Khan, W. (2014). Antimicrobial Polymers. Adv. Healthcare Mater. *3*, 1969–1985.

18. Taormina, G., Sciancalepore, C., Bondioli, F., and Messori, M. (2018). Special Resins for Stereolithography: In Situ Generation of Silver Nanoparticles. Polymers *10*, 212.

19. Podstawczyk, D., Skrzypczak, D., Połomska, X., Stargała, A., Witek-Krowiak, A., Guiseppi-Elie, A., and Galewski, Z. (2020). Preparation of antimicrobial 3D printing filament: In situ thermal formation of silver nanoparticles during the material extrusion. Polym. Compos. *41*, 4692–4705.

20. Bergonzi, C., Remaggi, G., Graiff, C., Bergamonti, L., Potenza, M., Ossiprandi, M.C., Zanotti, I., Bernini, F., Bettini, R., and Elviri, L. (2020). Three-Dimensional (3D) Printed Silver Nanoparticles/Alginate/Nanocrystalline Cellulose Hydrogels: Study of the Antimicrobial and Cytotoxicity Efficacy. Nanomaterials *10*, 844.

21. Vidakis, N., Petousis, M., Velidakis, E., Liebscher, M., and Tzounis, L. (2020). Three-Dimensional Printed Antimicrobial Objects of Polylactic Acid (PLA)-Silver Nanoparticle Nanocomposite Filaments Produced by an In-Situ Reduction Reactive Melt Mixing Process. Biomimetics *5*, 42.

22. Fantino, E., Chiappone, A., Roppolo, I., Manfredi, D., Bongiovanni, R., Pirri, C.F., and Calignano, F. (2016). 3D Printing of Conductive Complex Structures with In Situ Generation of Silver Nanoparticles. Adv. Mater. *28*, 3712–3717.

23. Prabhu Charan, K.T., Pothanagandhi, N., Vijayakrishna, K., Sivaramakrishna, A., Mecerreyes, D., and Sreedhar, B. (2014). Poly(ionic liquids) as "smart" stabilizers for metal nanoparticles. Eur. Polym. J. *60*, 114–122.

24. Dupont, J., and Scholten, J.D. (2010). On the structural and surface properties of transition-metal nanoparticles in ionic liquids. Chem. Soc. Rev. *39*, 1780–1804.

25. Muñoz-Bonilla, A., and Fernández-García, M. (2018). Poly(ionic liquid)s as antimicrobial materials. Eur. Polym. J. *105*, 135–149.

26. Zhang, T., Guo, J., Ding, Y., Mao, H., and Yan, F. (2019). Redox-responsive ferrocene-containing poly(ionic liquid)s for antibacterial applications. Sci. China Chem. *62*, 95–104.

27. Guo, J., Xu, Q., Zheng, Z., Zhou, S., Mao, H., Wang, B., and Yan, F. (2015). Intrinsically Antibacterial Poly(ionic liquid) Membranes: The Synergistic Effect of Anions. ACS Macro Lett. *4*, 1094–1098.

28. Fang, H., Wang, J., Li, L., Xu, L., Wu, Y., Wang, Y., Fei, X., Tian, J., and Li, Y. (2019). A novel high-strength poly(ionic liquid)/PVA hydrogel dressing for antibacterial applications. Chem. Eng. J. *365*, 153–164.

29. Bacon, S.L., Ross, R.J., Daugulis, A.J., and Parent, J.S. (2017). Imidazolium-based polyionic liquid absorbents for bioproduct recovery. Green Chem. *19*, 5203–5213.

30. Qian, L., Hu, X., Guan, P., Gao, B., Li, J., Wang, C., and Tang, Y. (2014). Preparation of bovine serum albumin imprinting sensitive hydrogels using ionic liquid as co-monomer and stabilizer. Talanta *121*, 56–64.

31. Isik, M., Gracia, R., Kollnus, L.C., Tomé, L.C., Marrucho, I.M., and Mecerreyes, D. (2013). Cholinium-Based Poly(ionic liquid)s: Synthesis, Characterization, and Application as Biocompatible Ion Gels and Cellulose Coatings. ACS Macro Lett. *2*, 975–979.

32. Claus, J., Brietzke, A., Lehnert, C., Oschatz, S., Grabow, N., and Kragl, U. (2020). Swelling characteristics and biocompatibility of ionic liquid based hydrogels for biomedical applications. PLoS One *15*, e0231421.

33. Qin, J., Guo, J., Xu, Q., Zheng, Z., Mao, H., and Yan, F. (2017). Synthesis of Pyrrolidinium-Type Poly(ionic liquid) Membranes for Antibacterial Applications. ACS Appl. Mater. Interfaces 9, 10504–10511.

34. He, B., Du, Y., Wang, B., Wang, X., Ye, Q., and Liu, S. (2021). Grafting embedded poly(ionic liquid) brushes on biomimetic sharklet resin surface for anti-biofouling applications. Prog. Org. Coating 157, 106298.

35. Li, Z., Wang, C., Qiu, W., and Liu, R. (2019). Antimicrobial Thiol–ene–acrylate Photosensitive Resins for DLP 3D Printing. Photochem. Photobiol. 95, 1219–1229.

36. Miralles-Comins, S., Zanatta, M., and Sans, V. (2022). Advanced Formulations Based on Poly(ionic liquid) Materials for Additive Manufacturing. Polymers 14, 5121.

37. Wales, D.J., Miralles-Comins, S., Franco-Castillo, I., Cameron, J.M., Cao, Q., Karjalainen, E., Alves Fernandes, J., Newton, G.N., Mitchell, S.G., and Sans, V. (2021). Decoupling manufacturing from application in additive manufactured antimicrobial materials. Biomater. Sci. 9, 5397–5406.

38. Mao, B.-H., Chen, Z.-Y., Wang, Y.-J., and Yan, S.-J. (2018). Silver nanoparticles have lethal and sublethal adverse effects on development and longevity by inducing ROS-mediated stress responses. Sci. Rep. 8, 2445.

39. Bondarenko, O., Juganson, K., Ivask, A., Kasemets, K., Mortimer, M., and Kahru, A. (2013). Toxicity of Ag, CuO and ZnO nanoparticles to selected environmentally relevant test organisms and mammalian cells in vitro: a critical review. Arch. Toxicol. 87, 1181–1200.

40. Grass, G., Rensing, C., and Solioz, M. (2011). Metallic copper as an antimicrobial surface. Appl. Environ. Microbiol. 77, 1541–1547.

41. Ren, G., Hu, D., Cheng, E.W.C., Vargas-Reus, M.A., Reip, P., and Allaker, R.P. (2009). Characterisation of copper oxide nanoparticles for antimicrobial applications. Int. J. Antimicrob. Agents 33, 587–590.

42. Nassar, M.A.Y., Eldien, H.M.S., Tawab, H.S.A., Saleem, T.H., Omar, H.M., Nassar, A.Y., and Hussein, M.R.A. (2012). Time-dependent Morphological and Biochemical Changes following Cutaneous Thermal Burn Injury and Their Modulation by Copper Nicotinate Complex: An Animal Model. Ultrastruct. Pathol. 36, 343–355.

43. Vincent, M., Duval, R.E., Hartemann, P., and Engels-Deutsch, M. (2018). Contact killing and antimicrobial properties of copper. J. Appl. Microbiol. 124, 1032–1046.

44. Ahamed, M., Alhadlaq, H.A., Khan, M.A.M., Karuppiah, P., and Al-Dhabi, N.A. (2014). Synthesis, Characterization, and Antimicrobial Activity of Copper Oxide Nanoparticles. J. Nanomater. 2014, 1–4.

45. Zuniga, J. (2018). 3D Printed Antibacterial Prostheses. Appl. Sci. 8, 1651.

46. Palza, H., Quijada, R., and Delgado, K. (2015). Antimicrobial polymer composites with copper micro- and nanoparticles: Effect of particle size and polymer matrix. J. Bioact. Compat Polym. 30, 366–380.

47. Palza, H., Nuñez, M., Bastías, R., and Delgado, K. (2018). In situ antimicrobial behavior of materials with copper-based additives in a hospital environment. Int. J. Antimicrob. Agents 51, 912–917.

48. Zuniga, J.M., and Cortes, A. (2020). The role of additive manufacturing and antimicrobial polymers in the COVID-19 pandemic. Expet Rev. Med. Dev. 17, 477–481.

49. González-Henríquez, C.M., Sarabia-Vallejos, M.A., and Rodríguez Hernandez, J. (2019). Antimicrobial Polymers for Additive Manufacturing. Int. J. Mol. Sci. 20, 1210.

50. Muwaffak, Z., Goyanes, A., Clark, V., Basit, A.W., Hilton, S.T., and Gaisford, S. (2017). Patient-specific 3D scanned and 3D printed antimicrobial polycaprolactone wound dressings. Int. J. Pharm. 527, 161–170.

51. Zheng, Z., Guo, J., Mao, H., Xu, Q., Qin, J., and Yan, F. (2017). Metal-Containing Poly(ionic liquid) Membranes for Antibacterial Applications. ACS Biomater. Sci. Eng. 3, 922–928.

52. Ameh, T., and Sayes, C.M. (2019). The potential exposure and hazards of copper nanoparticles: A review. Environ. Toxicol. Pharmacol. 71, 103220.

53. Thit, A., Sandgaard, M.H., Sturve, J., Mouneyrac, C., Baun, A., and Selck, H. (2021). Influence of Aging on Bioaccumulation and Toxicity of Copper Oxide Nanoparticles and Dissolved Copper in the Sediment-Dwelling Oligochaete Tubifex tubifex: A Long-Term Study Using a Stable Copper Isotope. Front. Toxicol. 3, 737158.

54. Budiyanti, D.S., Moeller, M.E., and Thit, A. (2022). Influence of copper treatment on bioaccumulation, survival, behavior, and fecundity in the fruit fly Drosophila melanogaster: Toxicity of copper oxide nanoparticles differ from dissolved copper. Environ. Toxicol. Pharmacol. 92, 103852.

55. Recalde, I.B., Recalde, D., García-Lopera, R., and Gómez, C.M. (2005). FTIR isothermal cure kinetics and morphology of dicyanate ester resin/polysulfone blends. Eur. Polym. J. 41, 2635–2643.

56. Akitsu, T., Yamaguchi, J., Uchida, N., and Aritake, Y. (2009). The Studies of Conditions for Inducing Chirality to Cu(II) Complexes by Chiral Zn(II) and Ni(II) Complexes with Schiff Base. Research Letters in Materials Science 2009, 1–4.

57. Wang, M., Zhang, Q., Xie, Q., Wan, L., Zhao, Y., Zhang, X., and Luo, J. (2020). Selective electrochemical reduction of carbon dioxide to ethylene on a copper hydroxide nitrate nanostructure electrode. Nanoscale 12, 17013–17019.

58. Copper (Cu) Compounds. Copper (II) Nitrate (CuNO3). https://xpsdatabase.com/copper-spectra-cuno3/.

59. Bacchella, C., Dell'Acqua, S., Nicolis, S., Monzani, E., and Casella, L. (2021). A Cu-bis(imidazole) Substrate Intermediate Is the Catalytically Competent Center for Catechol Oxidase Activity of Copper Amyloid-β. Inorg. Chem. 60, 606–613.

60. Bete, S.C., Würtele, C., and Otte, M. (2019). A bio-inspired imidazole-functionalised copper cage complex. Chem. Commun. 55, 4427–4430.

61. Zhang, Z., Gao, H., Wu, H., Qian, Y., Chen, L., and Chen, J. (2018). Chemical Fixation of CO2 by Using Carbon Material-Grafted N-Heterocyclic Carbene Silver and Copper Complexes. ACS Appl. Nano Mater. 1, 6463–6476.

62. Gawande, M.B., Goswami, A., Felpin, F.-X., Asefa, T., Huang, X., Silva, R., Zou, X., Zboril, R., and Varma, R.S. (2016). Cu and Cu-Based Nanoparticles: Synthesis and Applications in Catalysis. Chem. Rev. 116, 3722–3811.

63. Schildermans, I., Mullens, J., Van der Veken, B.J., Yperman, J., Franco, D., and Van Poucke, L.C. (1993). Preparation and thermal decomposition of Cu2(OH)3NO3. Thermochim. Acta 224, 227–232.

64. Liu, X., Geng, B., Du, Q., Ma, J., and Liu, X. (2007). Temperature-controlled self-assembled synthesis of CuO, Cu2O and Cu nanoparticles through a single-precursor route. Mater. Sci. Eng. 448, 7–14.

65. Ranjbar-Karimi, R., Bazmandegan-Shamili, A., Aslani, A., and Kaviani, K. (2010). Sonochemical synthesis, characterization and thermal and optical analysis of CuO nanoparticles. Phys. B Condens. Matter 405, 3096–3100.

66. Das, D., Nath, B.C., Phukon, P., and Dolui, S.K. (2013). Synthesis and evaluation of antioxidant and antibacterial behavior of CuO nanoparticles. Colloids Surf. B Biointerfaces 101, 430–433.

67. Calabro, R.L., Burpo, F.J., Bartolucci, S.F., and Maurer, J.A. (2023). Seed-Mediated Growth of Oxidation-Resistant Copper Nanoparticles. J. Phys. Chem. C 127, 15307–15315.

68. Dulta, K., Koşarsoy Ağçeli, G., Chauhan, P., Jasrotia, R., Chauhan, P.K., and Ighalo, J.O. (2022). Multifunctional CuO nanoparticles with enhanced photocatalytic dye degradation and antibacterial activity. Sustain. Environ. Res. 32, 2.

69. Miralles-Comins, S., Zanatta, M., Gualdrón-Reyes, A.F., Rodriguez-Pereira, J., Mora-Seró, I., and Sans, V. (2023). Polymeric ionic liquid-based formulations for the fabrication of highly stable perovskite nanocrystal composites for photocatalytic applications. Nanoscale 15, 4962–4971.

70. Luo, Z., Cui, H., Guo, J., Yao, J., Fang, X., Yan, F., Wang, B., and Mao, H. (2021). Poly(ionic liquid)/Ce-Based Antimicrobial Nanofibrous Membrane for Blocking Drug-Resistance Dissemination from MRSA-Infected Wounds. Adv. Funct. Mater. 31, 2100336.

71. (2016). Standard Test Methods for Determination of Gel Content and Swell Ratio of Crosslinked Ethylene Plastics. https://www.astm.org/d2765-16.html.